HEALTH AND MEDICINE

Experimental and theoretical explorations of nanocarriers' multistep delivery performance for rational design and anticancer prediction

Weier Bao[1,2]*, Falin Tian[3]*, Chengliang Lyu[2]*, Bin Liu[1]*, Bin Li[3], Luyao Zhang[3], Xianwu Liu[1,2], Feng Li[2], Dan Li[1], Xiaoyong Gao[2], Shuo Wang[2], Wei Wei[2,4†], Xinghua Shi[3,4†], Yuan Li[1†]

The poor understanding of the complex multistep process taken by nanocarriers during the delivery process limits the delivery efficiencies and further hinders the translation of these systems into medicine. Here, we describe a series of six self-assembled nanocarrier types with systematically altered physical properties including size, shape, and rigidity, as well as both in vitro and in vivo analyses of their performance in blood circulation, tumor penetration, cancer cell uptake, and anticancer efficacy. We also developed both data and simulation-based models for understanding the influence of physical properties, both individually and considered together, on each delivery step and overall delivery process. Thus, beyond finding that nanocarriers that are simultaneously endowed with tubular shape, short length, and low rigidity outperformed the other types, we now have a suit of theoretical models that can predict how nanocarrier properties will individually and collectively perform in the multistep delivery of anticancer therapies.

INTRODUCTION

Nanocarrier-based drug delivery platforms have emerged as attractive tools for delivering anticancer drugs into tumors, where they can exploit the pathophysiological conditions of the tumor to specifically deliver drugs (1, 2). Many nanocarriers such as gold nanoparticles and liposome are produced as colloidal delivery vehicles with particle sizes typically around 10 to 200 nm (3, 4). Although these nanocarriers show promising results in vitro, they still have to face a complex series of biological barriers after they entered the body (5–8). It has been reported that the effective delivery rate of medical nanoparticles into solid tumors may represent less than 1% of the administered doses, which substantially limited the clinical translation of these materials into medicine (9). Thus, there is a growing awareness that we need to improve our understanding of the factors that contribute to poor delivery efficiency and of the nanoscale interactions between nanocarriers and biological systems if we want to develop new nanocarrier materials and platforms that can achieve high delivery efficiency.

Many studies have explored nanomaterials with diverse properties seeking to understanding nanocarrier-biological interaction mechanisms, with the aim of reducing physical barriers and physiological hurdles and increasing the delivery efficiency of nanocarriers, especially into tumors (10–14). However, most of these studies have focused on a single aspect of the delivery process, for example, blood circulation dynamics (15, 16), extracellular matrix penetration (17),

or cellular uptake (18), producing results and prediction models that often conflict or contradict findings from other authors. For instance, according to the Stokes-Einstein equation, decreasing the size of the nanocarriers leads to an increased diffusion coefficient and further improves their diffusion ability in the extracellular matrix of tumor. However, with the Helfrich membrane elastic model, smaller nanocarriers need to overcome higher membrane deformation energy during cellular uptake, yielding inefficient cellular uptake (19, 20). In the aspect of nanocarrier rigidity on the effect of delivery efficiency, based on combined experimental data and molecular simulations, Sun et al. (21) concluded that the rigidity of nanocarriers can markedly alter their cellular uptake efficiency, reporting that highly rigid nanocarriers able to pass through cell membranes more easily. In contrast, a recent study showed that cellular uptake efficiency of highly rigid nanocarriers was lower than for semirigid nanocarriers when the cell was covered by a matrix layer (22).

In general, it is agreed that the transport of therapeutic nanocarriers from blood circulation into cancer cells is a sequential process comprising the following steps: Nanocarriers flow via blood circulation to tumor sites, cross the vessel wall, then begin to penetrate into the interior of the solid tumor (to varying depths), and are lastly taken up into target cells via diverse mechanisms depending on the physiochemical properties of the nanocarriers (23). There is, at present, a lack of design principles—for each transport phase individually and for the overall process as an integrated whole—to guide the design of nanomaterials with combinations of properties predicted to offer efficient delivery performance (9).

Seeking to rigorously characterize and thus better understand the contributions of particular properties of nanocarriers on their delivery performance, we here developed a set of six self-assembled nanocarrier types prepared from hydrolyzed peptide fragments of α-lactalbumin (α-lac) to use as a "test bed" in which we could systematically alter physical properties. We altered nanocarrier size, shape, and rigidity, and we conducted both experiments and simulations to explore the performance of each type of nanocarriers in blood circulation and intratumoral invasion, which included both tumor

[1]Key Laboratory of Precision Nutrition and Food Quality, Key Laboratory of Functional Dairy, College of Food Science and Nutritional Engineering, China Agricultural University, Beijing 100083, P. R. China. [2]State Key Laboratory of Biochemical Engineering, Institute of Process Engineering, Chinese Academy of Sciences, Beijing 100190, P. R. China. [3]Laboratory of Theoretical and Computational Nanoscience, Chinese Academy of Sciences (CAS) Key Laboratory for Nanosystem and Hierarchy Fabrication, CAS Center for Excellence in Nanoscience, National Center for Nanoscience and Technology, Chinese Academy of Sciences, Beijing 100190, P. R. China. [4]University of Chinese Academy of Sciences, No. 19A Yuquan Road, Beijing 100049, P. R. China.
*These authors contributed equally to this work.
†Corresponding author. Email: yuanli@cau.edu.cn (Y.L.); weiwei@ipe.ac.cn (W.W.); shixh@nanoctr.cn (X.S.)

penetration and cancer cell uptake. Specifically, we combined data from experiments using cancer cell lines, tumor cell spheroids, mice, and xenograft tumor models with multiple coarse-grained molecular dynamics (CGMD) simulations and generated a suite of theoretical models to evaluate the impacts of multiple physical properties, including several models for blood pharmacodynamics, intratumoral penetration, cancer cell uptake, and an integrated theoretical model for overall delivery efficiency (Fig. 1). We believe that the data, simulations, and models are helpful to unseal and predict nanocarrier perform in multistep delivery for anticancer therapy.

RESULTS

### Production of nanocarriers with systematically altered physical properties

Previous studies have investigated the effects of the individual physical property of nanocarriers on their delivery performance (24, 25). For systematical and accurate investigation of the relationship between multiple physical properties and delivery performance, a critical prerequisite is the construction of nanocarriers with identical material but diverse and univariate physical properties. To this end, we developed a set nanocarrier types with differing physical properties that were variously produced from hydrolyzed peptide fragments of α-lac. That is, building from previous understanding about how these α-lac peptide fragments can undergo a self-assembly process to produce nanostructures (26, 27), we here systematically altered three separate production conditions to produce six different types of nanocarriers from the same starting material. The first condition that we altered was the controlled shape of the nanocarriers. It is known that altering the concentration of Ca²⁺ ions in the production solution can control whether the α-lac peptide fragments self-assemble into nanospheres (NS) or nanotubes (NT) based on differential

Ca²⁺ coordination dynamics. The second production condition that we altered was the inclusion or exclusion of a sonication step to control the size of the nanocarriers: This step fragmented the self-assembled "long" NTs (LNTs; ~1000 nm in length) into "short" NTs (SNTs; ~200 nm in length) (fig. S1A). Last, we were able to control the rigidity of the variously shaped and variously sized nanocarriers by selectively subjected them to a glutaraldehyde for cross-linking the amino group inside. On the basis of identical material, we were thus able to generate NSs, cross-linked NSs (CNSs), SNTs, cross-linked SNTs (CSNTs), LNTs, and cross-linked LNTs (CLNTs).

Transmission electron microscope (TEM), atomic force microscope (AFM), and dynamic light scattering analyses (Fig. 2, A and C) revealed that all six α-lac nanocarrier types had an equal diameter of ~20 nm. The sonication step produced NTs with lengths of ~200 or ~1000 nm. Moreover, cross-linking step had almost no effect on nanocarrier morphology (Fig. 2A), or surface charge density in Fig. 2D, while increased nanocarrier rigidity by about threefold in all of the paired cases (assessed as the Young's modulus; Fig. 2B and fig. S1B), i.e., from ~400 to ~1200 MPa after cross-linking for NS versus CNS, etc. Note that these nanocarriers had narrow size distribution with almost no overlay, which could assure the certainty for further simulations and experiments. Meanwhile, all these nanocarriers exhibited constant size during 1-week storage in the cell culture medium, demonstrating their favorable stability for intravenous injection (fig. S1C). Moreover, we loaded the chemotherapy agent doxorubicin (Dox) into the hydrophobic domain of each of the six nanocarrier types. Compared with naked nanocarriers, the results showed that the loading of the Dox has few effects on the size, charge, or rigidity (fig. S1, D to F). In addition, none of the empty nanocarrier types exerted cytotoxicity on in vitro [incubation time, 24 to 72 hours; dose range, 0 to 100 μg/ml; cell types, breast cancer cells (4T1), mouse macrophage cells (J774A.1), mouse primary macrophages, mouse
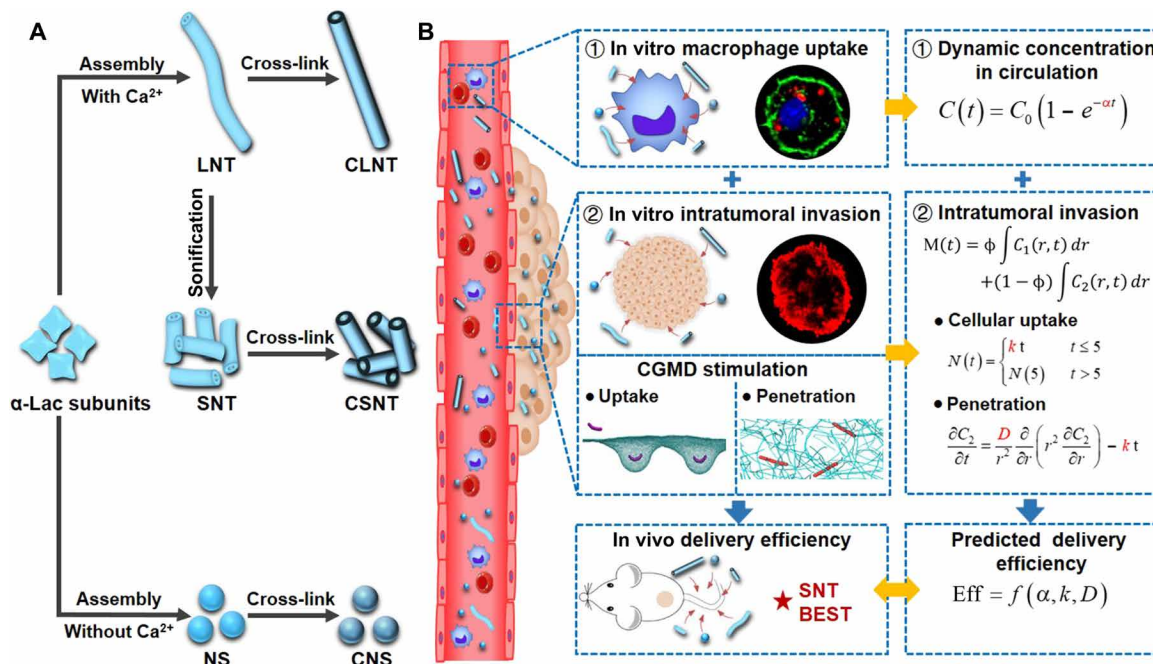
Fig. 1. Schematic illustration of the construction of six self-assembled nanocarrier types and prediction for overall delivery efficiency in vivo through experiments in vitro and simulation analysis. (**A**) The production of six different types of nanocarriers with various physical properties (size, shape, and rigidity). These nanocarriers from the same starting material (α-Lac) were produced by three separate production conditions (the concerntration of Ca²⁺, sonication, and cross-linking). (**B**) In vivo predicted delivery efficiency evaluated by in vitro experimental data and simulation analysis. The Eff means the predicted ratio of the total accumulation of various nanocarriers at the tumor site over time to the injected dose.
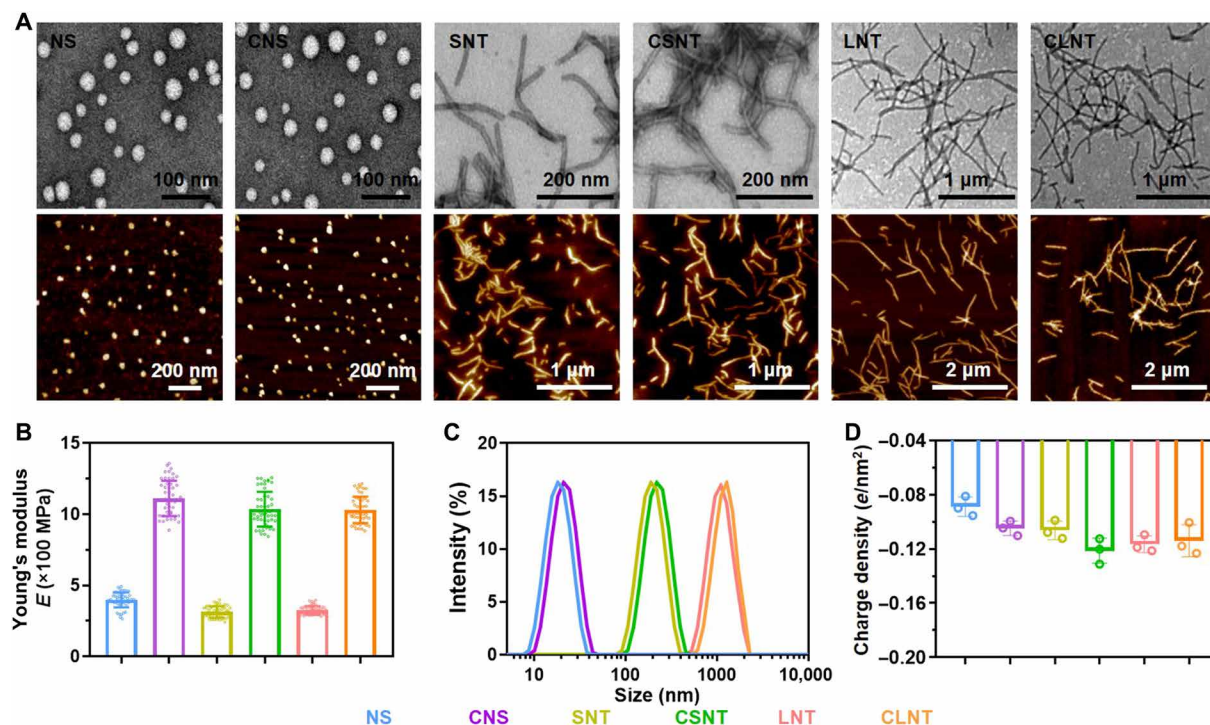
Fig. 2. Characterizations of α-lac nanocarriers. (**A**) TEM and AFM images of various nanocarriers. (**B**) Young's modulus E (×100 MPa) of various nanocarriers measured by AFM. Data represent the means ± SD ($n = 50$). (**C**) Size distribution of various nanocarriers in phosphate-buffered saline (PBS). (**D**) Surface charge density of various nanocarriers. Data represent the means ± SD ($n = 3$).

macrophage cells (RAW 264.7), human cervical cancer cells (HeLa), and human umbilical vein endothelial cells (HUVECs)] and in vivo (healthy Balb/c mice) in fig. S2 (A to E). Such a good biocompatibility of these nanocarriers will facilitate our comparative investigation.

Effects of nanocarrier physical properties on macrophage capture and blood circulation

Given our goal of applying these nanocarriers to in vivo antitumor drug delivery applications, we next evaluated their circulation in mice. Recall that the ability of intravenously delivered nanocarriers to deliver their cargo ultimately requires their arrival at a targeted site and that the propensity for successful targeting therefore depends on their circulation in blood. We assessed their overall circulation dynamics using a combination of standard in vitro macrophage capture assays and blood pharmacokinetics experiment. It is now well established that macrophages act as effective scavengers for foreign nanomaterials in circulating blood (28, 29). Upon various uptake pathways, macrophages exhibited distinct appetites to these nanocarriers with univariate physical properties. We produced the six nanocarrier types harboring the fluorescent dye Cy5 as cargo and used them in 36-hour assays with 10,000 macrophages exposed to varying concentrations of each nanocarrier type. Flow cytometry (FCM)–based Cy5 signal intensity measurement enabled quantification and generation of time/dose-dependent uptake profiles, which we present as three-dimensional (3D) parametric graphs. Fundamentally, this analysis indicated that the sequence (from least to most likely) of macrophage capture (assessed as Y_{max}) was NS, SNT, CNS, LNT, CSNT, and CLNT. Similar tendency was also observed in the images captured by confocal laser scanning microscopy (CLSM), again suggesting that the physical properties of spherical shape, low rigidity,

and short size were the favorable physical properties for avoiding scavenging by macrophages (Fig. 3A). These results were further verified by primary macrophage and RAW 264.7 cell lines (fig. S3, A and B).

We also intravenously injected Balb/c mice with Cy5-harboring nanocarriers of all six types and used analytical process of Cy5 signal in whole blood to facilitate standard pharmacokinetics analysis of blood. This analysis revealed that the circulation time in the mouse circulatory system followed the same trend that we had observed in the macrophage capture assays, with spherical, nonrigid, and short nanocarriers apparently having the most favorable physical properties for prolonged circulation time (Fig. 3B). Correspondingly, the half-life period ($T_{1/2}$) values for the nanocarrier types followed the same order, with NS exhibiting the maximal value of ~18.9 hours (Fig. 3C). Notably, these $T_{1/2}$ values in vivo showed positive correlation ($R^2 = 0.8025$) with in vitro α value, which was fitted by a first-order decay kinetics model with the J774A.1 macrophage uptake assay data (fig. S5A). Similar positive correlation relationships were further found on other two types of macrophages (primary macrophage and RAW 264.7) (fig. S3, C and D). This finding thus emphasized the reliability of using in vitro data to predict in vivo circulation fates for these nanomaterials (Fig. 3D). Upon this fitting, the simple equation was used to simplify this complicated process, and further, a parameter (α) was used for the prediction of in vivo circulation.

Evaluation of nanocarrier physical properties on intratumoral invasion

Having demonstrated that various nanocarriers exhibited differential retention properties in blood, we next assessed their capacity for intratumoral invasion. Subsequently, we use the multicellular tumor
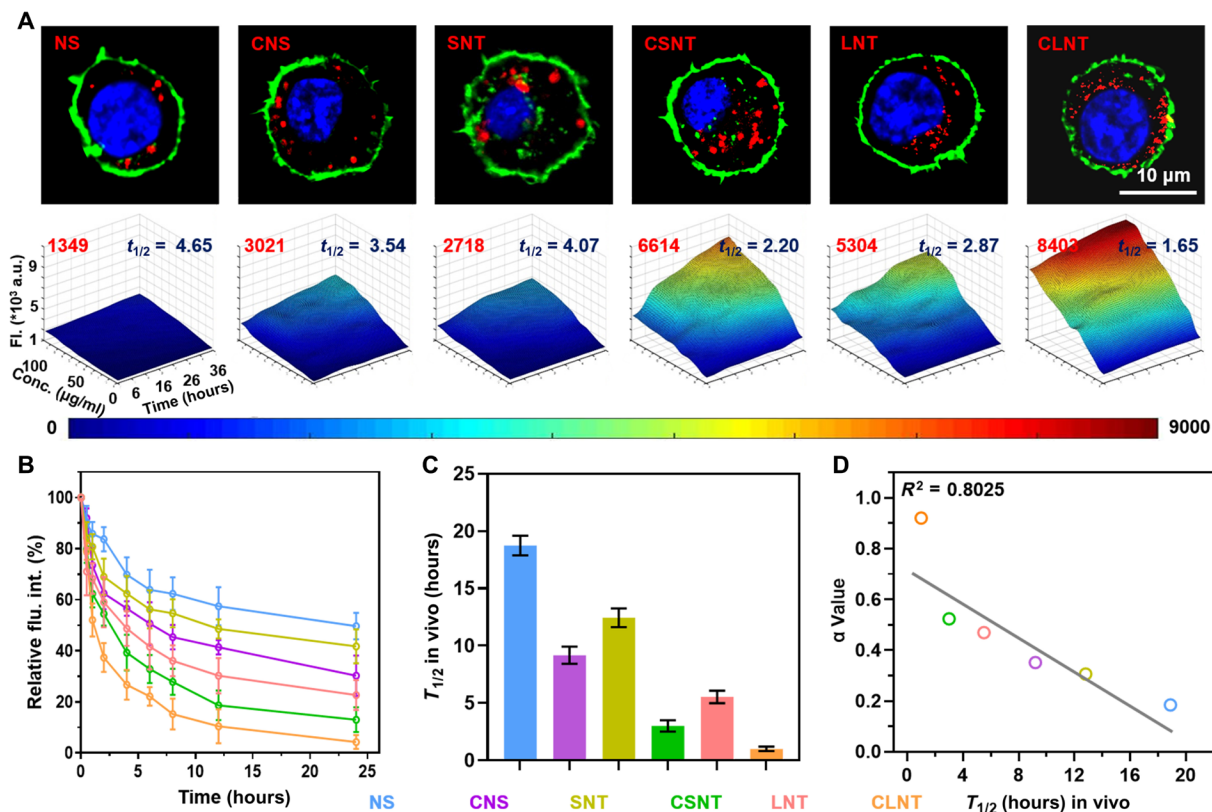
Fig. 3. Effects of nanocarrier physical properties on macrophage capture and blood circulation. (**A**) CLSM images and FCM analysis of nanocarriers in J774A.1 cells with different times and doses. $t_{1/2}$ represents the time of the half maximum uptake. Green, cell membrane; blue, nucleus; red, nanocarriers. a.u., arbitrary units; FI, fluorescence intensity. (**B**) Pharmacokinetic profiles of nanocarriers in blood. flu. int., fluorescence intensity. (**C**) The half-life time ($T_{1/2}$) of nanocarriers in vivo. (**D**) Correlation analysis of α value in vitro and $T_{1/2}$ in vivo. Data in (B) and (C) represent the means ± SD ($n = 3$).

spheroids (MCTSs) to mimic the microenvironment of the tumor because of the tightly packed cell population and extracellular matrix (*30–32*). Moreover, the MCTS is also more suitable and convenient for the design and data extrapolation of nanocarriers. Simply, the 4T1 MCTSs were initially seeded with around 2000 cells per well, and after 4 days of culture, they had reached about 500 μm in diameter, at which point they were treated for different time durations with Cy5-harboring nanocarriers of each of the six types.

The CLSM images in Fig. 4A indicated that the MCTS invasion abilities of the different nanocarrier types differed greatly and strongly suggested that smaller size and reduced rigidity are particularly influential physical properties in terms of spheroid invasion. Specifically, we found that whereas the long and rigid nanocarriers (e.g., CSNT, LNT, and CLNT) only had observable signals around the outmost layers of the MCTS (Fig. 4A), SNT signals were evident in the deep areas of the spheroids, outperforming each of the other types. Beyond the obvious trends from the images, quantitation of the total fluorescence intensity of each MCTS and the inward coefficient further confirmed the superior MCTS invasion ability of the SNT nanocarriers.

Simulations and theoretical model for intratumoral invasion

During the invasion process, the nanocarriers should also have efficient uptake by cancer cell and deep penetration within extracellular matrix. Definitely, these two aspects are closely interrelated, but the traditional

experiments omitted this and often investigated them individually. To this end, we constructed and performed a series of CGMD simulations for a deeper insight about the interrelated and complex relationship between penetration and cellular uptake during nanocarriers' intratumoral invasion. In the "cancer cell uptake dynamics" (CCUD) simulation, the system is composed of a piece of lipid membrane and modeled versions of each nanocarrier type (see details in Materials and Methods and fig. S4, A to D) (*33, 34*). We ran CCUD simulations and revealed the cellular uptake processes of the various nanocarriers, which could be verified by FCM and CLSM experimental data (fig. S4, E and F). Both spherical nanocarrier types (NS and CNS) could be fully engulfed by the membrane in a short time (CNS, ~500 μs; NS, ~750 μs). The tubular CSNT type could also be fully engulfed, but this required a longer time (~1550 μs) accompanied by a remarkable rotation during the uptake process. Simulation of the SNTs suggested that they could be fully wrapped after ~2380 μs and intriguingly revealed that the structure of these nanocarriers undergoes an obvious shape change during the cellular uptake process. For the long tubular nanocarriers (LNT and CLNT), they had not been extensively wrapped after a relatively long time (longer than ~3000 μs), suggesting that the large size limits their uptake by membranes (Fig. 4B and fig. S4, G and H).

To elucidate the inward penetration within extracellular matrix, we continued to conduct another additional CGMD simulations [named "tumor extracellular diffusivity" (TED) simulation] with a
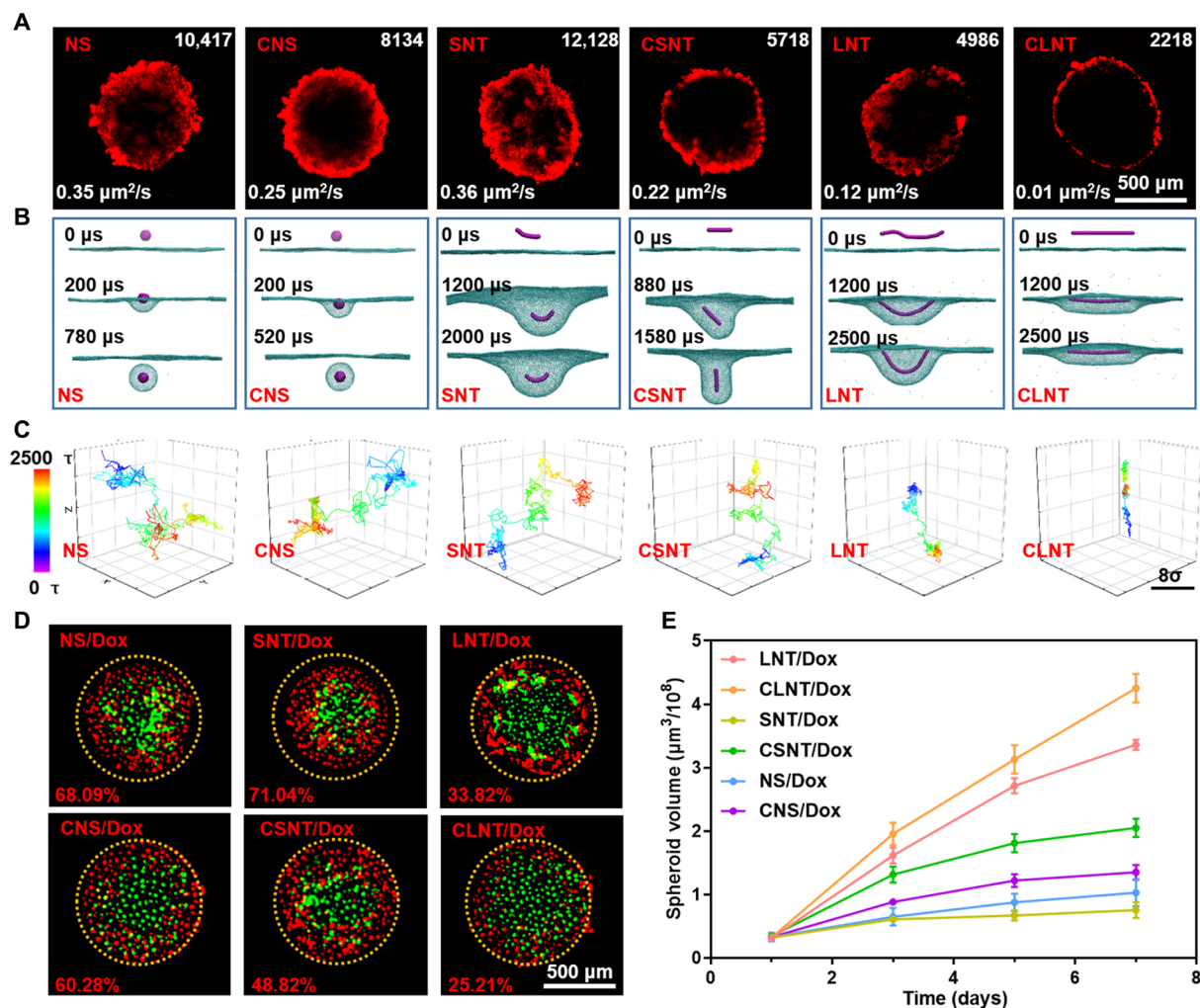
Fig. 4. Evaluation and simulation of nanocarrier physical properties on intratumoral invasion. (**A**) CLSM images and corresponding quantification of the invasion of different nanocarriers in 4T1 MCTSs after 24 hours. Quantitation of the total fluorescence intensity (right top) of each MCTS and the apparent diffusion coefficient (left bottom) were calculated and analyzed. Red, nanocarriers. (**B**) CGMD simulation for the cellular uptake processes of various nanocarriers. (**C**) CGMD simulation for 3D trajectories of various nanocarriers' diffusion in tumor matrix, with the color maps of simulation times. The scale bar and the grid size are 8σ. (**D**) CLSM images of terminal deoxynucleotidyl transferase–mediated deoxyuridine triphosphate nick end labeling (TUNEL) analysis of 4T1 spheroids after treatment with different nanocarriers/Dox. Green, live cells; red, apoptosis cells. (**E**) The inhibitory effect on the growth curve of 4T1 spheroids of nanocarriers/Dox. Data in (E) represent the means ± SD (n = 3).

model system, in which a linked random polymer network represented the structure of the extracellular matrix in tumor (fig. S4) (*35*). These TED simulations succeeded in monitoring 3D centroid trajectories of the diffusion of the six nanocarriers in the polymer network. Compared with other counterparts, SNT nanocarriers were thus able to occupy the largest overall volume of the simulation box with the highest mean square displacement (MSD) (Fig. 4C and fig. S4I). Such a superior migration capacity within extracellular matrix could be attributed to moderate aspect ratios and low rigidity. Obviously, the large size of the LNTs and CLNTs significantly limited their diffusivity among the simulated polymer matrix (movies S1 and S2). Although the NS and CNS nanocarriers are smaller than the SNTs, the shape isotropy of these nanocarriers makes them trapped in the pores of the network due to the lacking of the rotational motion, which is driven by the heterogeneous adhesive interactions between nanocarriers and host polymer and is the key factor to improve the diffusivity of nanocarriers (*36*) (movies S5 and S6). In addition, the

low rigidity of non–cross-linked nanocarrier types further endowed them with the ability of self-modulate their shape to adjust to the network pores, therefore enhancing their overall migration (movies S3 and S4). Moreover, movie S1 represents Supplementary Video LNT. Movie S2 represents Supplementary Video CLNT. Movie S3 represents Supplementary Video SNT. Movie S4 represents Supplementary Video CSNT. Movie S5 represents Supplementary Video NS. Movie S6 represents Supplementary Video CNS.

Having unsealed the behaviors of each nanocarrier type on cancer cell uptake and extracellular matrix penetration, we next sought to investigate these interrelated aspects together using a theoretical model, which were based on the stacked image data of MCTS captured at different time points. Specifically, we were aiming to generate a function to model the radial distance traveled by a nanocarrier within the spheroid for specific time interval. Thus, a spherical radial diffusion function with special initial and boundary condition is used to describe the diffusion process of the nanocarriers in tumor

extracellular matrix. To additionally consider the contribution of cancer cell uptake in our model, we used an equation to fit the uptake rate from the cultured 4T1 uptake assay data (see details in Materials and Method and fig. S5B), and once we had a cancer cell uptake rate parameter for each type of nanocarriers, we were able to predict the number of particles uptake by each cell. Last, we combined the two data-derived models to build our theoretical model of intratumoral accumulation.

After obtaining the parameters for cancer cell uptake (k) and extracellular tumor matrix diffusion (D_M) in fig. S5 (C to E), we next used the intratumoral invasion model to calculate the concentration distribution of the nanocarriers in the tumor. As shown in fig. S5F, for all of the nanocarrier types, the highest concentrations were predicted to be occurred at the interface of the tumor spheroid with the surrounding medium ($r = R$, where R is the radius of the tumor), and the concentrations of all types decreased closer to the center of the tumor ($r = 0$). Specifically, SNT with a moderate engulfment efficacy by cell membrane and a much superior extracellular penetration together resulted in the prediction that they would extensively invade into the center of the tumor within a relatively short time window (less than 12 hours). On the contrary, CLNT with high aspect ratio and high rigidity only reside around the tumor surface and hardly invade into the core region of the tumor (even with extended time window modeling), owing to the most difficult engulfment by cell membrane and very low diffusivity within extracellular matrix.

To experimentally validate the utility of our theoretical intratumoral invasion model in predicting the delivery efficiency of nanocarrier cargoes into spheroid tumors, we loaded each of the six nanocarrier types with the chemotherapy agent Dox and treated 4T1 spheroids, which we subsequently assessed for evaluating apoptosis and inhibition on MCTS growth. As shown in Fig. 4D, the above-mentioned nanocarriers with various invasion abilities further led to distinct cytotoxic effect, which could be verified by the different amounts of apoptotic cells [determined by terminal deoxynucleotidyl transferase–mediated deoxyuridine triphosphate nick end labeling (TUNEL) assay] and their nonuniform distribution in MCTSs. Owing to the efficient invasion, SNT induced more extensive cell death (indicated by red color), resulting in remain of a few live cells in the core while exfoliating apoptotic cells at the outmost layer. On the other hand, the apoptotic rate gradually decreased in other groups, since the invasion was compromised with various extents. The different levels of apoptosis further resulted in significant disparity on the MCTSs growth inhibition (Fig. 4E and fig. S6A). The performance of the nanocarriers (assessed as growth inhibition rates) decreased in following sequence: SNT, NS, CNS, CSNT, LNT, and CLNT, which again support the smaller-size, nonrigid, tube-shaped properties as most advantageous for effective intratumoral invasion.

Evaluation and prediction of integral delivery efficiency in vivo

Given the apparent predictive utility for in vitro MCTS invasion of our theoretical model, we next complement and develop the model to evaluate the overall delivery efficiency from blood circulation into cancer cells. In this situation, the concentrations of the nanocarriers around the tumor are not fixed, which could change with the blood circulation. Therefore, obviously, circulation (and the impact of various physical properties on it) is also relevant parameters to consider. In this aspect, combination of blood pharmacokinetics model with our intratumoral invasion model to generate an integrated model is

required. To this end, we introduced the parameter β (obtained from the blood circulation experiment) and modified boundary conditions to the main model, which enabled us to predict a final overall delivery efficiency, as well as its performance information for three intermediate stages (circulation, intratumoral penetration, and cancer cell uptake). Actually, considering the relationship between blood half-life period ($T_{1/2}$) for the nanocarriers and macrophage uptake, we can predict the blood circulation of the nanocarriers using in vitro macrophage uptake α indirectly. That is, upon the hypothetical intravenous injection of a given nanocarrier structure, we can use this model to predict its in vivo overall delivery efficiency (denoted as prediction value of nanocarrier at tumor site) only using three parameters (α, k, and D) from in vitro tests.

As shown in Fig. 5A, the predicted circulation capacity of six nanocarrier type increased in the sequence of CLNT, CSNT, LNT, CNS, SNT, and NS. As the first delivery process after intravenous injection, the circulation of nanocarriers was mainly determined by the macrophage interception. In this case, our prediction for blood circulation trends is most informative in explaining the accumulation of nanocarriers in the liver and spleen. Although NS was predicted to perform best in the circulation stage and the cancer cell uptake stage, the drop of performance predicted in the intratumoral penetration stages leads to the compromised prediction value in tumor (Fig. 5B). On the contrary, SNT, even following the circulation, was still predicted to have the most efficient intratumoral penetration and a relative higher cancer cell uptake, thus taking the lead on the overall delivery efficiency. Once cross-linked, CSNT was predicted to show significant decrease in each stage and the prediction value, reflecting deleterious effect of high rigidity on the anticancer drug delivery.

To testify the utility of our integrated model, we next monitor the biodistribution of different nanocarriers in a 4T1-xenografted mouse model after intravenous injection. As foreign nanomaterials, all nanocarriers could be intercepted by macrophage in the liver and spleen with various degrees during the blood circulation (Fig. 5C and fig. S6B). The less interception at these two reticuloendothelial organs, the more accumulation at tumor site could be observed for these six nanocarrier types. Correspondingly, the signal intensity at tumor area increased in the sequence of CLNT, LNT, CSNT, CNS, NS, and SNT, which could also be verified by the brightness of euthanized tumor tissues after 120 hours (Fig. 5, D and E). With further quantification, the peak tumor-to-liver fluorescent intensity value achieved in SNT was 3.6 times higher compared to that in the CLNT group (fig. S6C), which again emphasized that the tubular shape, low rigidity, and small aspect ratio are the preferred physical properties in the aspect of integral delivery process. Notably, we observed theoretical prediction values were in the same order as the experimental values at tumor sites, again demonstrating that we can use the in vitro data for comparatively predicting the in vivo delivery efficiency (Fig. 5F).

Comparative evaluation of anticancer efficacy for various nanocarriers/Dox in vivo

Last, we were in the position to evaluate and verify the in vivo antitumor effects of these nanocarriers with distinct physical properties based on overall in vitro data. To this end, nanocarriers were loaded with Dox and intravenously injected into Balb/c mice bearing 4T1 tumor xenografts with the dose of equivalent Dox (0.5 mg/ml, 200 μl for each mouse). Compared with the rapid tumor development in
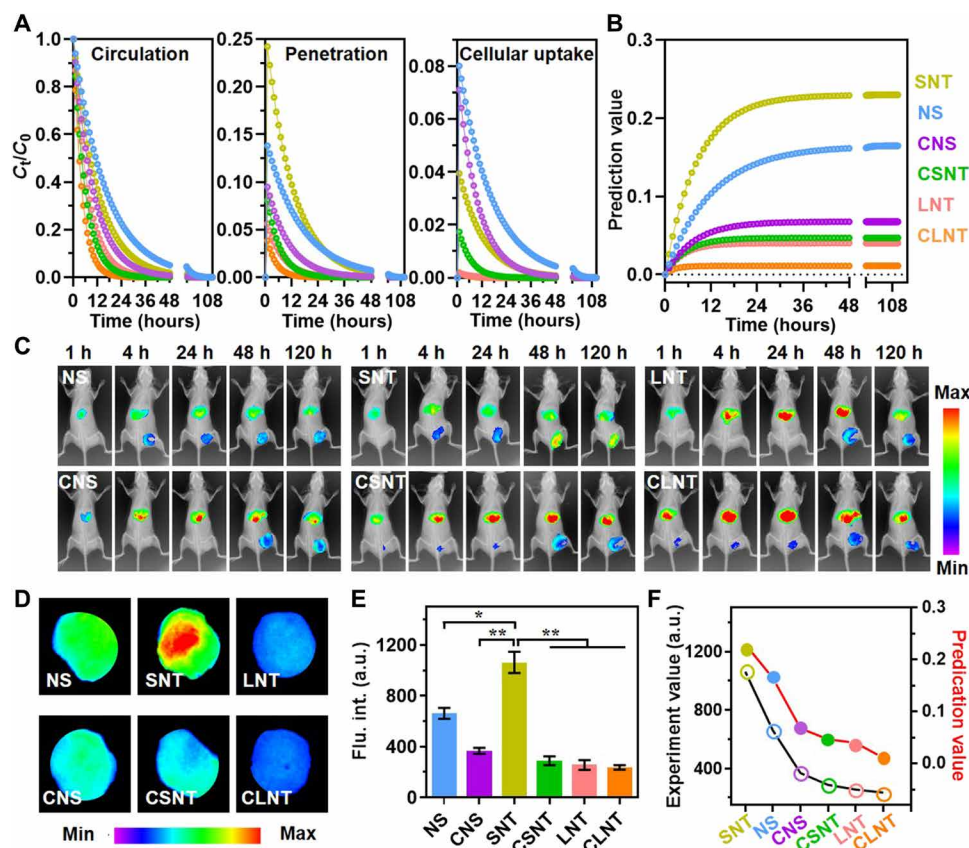
Fig. 5. Evaluation and prediction of integral delivery efficiency in vivo. (**A**) The calculated concentration profile of the different nanocarriers for different stages during the in vivo delivery process over time. (**B**) The prediction values of various nanocarriers in the HeLa tumor over time. (**C**) In vivo imaging of biodistribution of nanocarriers in tumor-xenografted mice model. (**D**) Ex vivo fluorescence imaging of tumors with different treatments after 120-hour nanocarrier injection. (**E**) The quantification of tumor fluorescence intensity after 120-hour intravenous injection of various formulations. (**F**) Theoretical prediction value and experimental value at tumor sites with various treatments. The experimental value and the prediction value at tumor sites showed the same order. Solid dots indicate the prediction values, and hollow dots indicate experiment value. Data in (E) represent the means ± SD ($n = 6$). Statistical significance between multiple groups was calculated using one-way analysis of variance (ANOVA) for (E). *$P < 0.05$ and **$P < 0.01$.

the phosphate-buffered saline (PBS) group, free Dox failed to inhibit tumor growth (Fig. 6A). This could be ameliorated in various degrees by the delivery with nanocarriers. Specifically, SNT/Dox with a most superior delivery performance significantly outperformed other counterparts on suppression of tumor development and had almost no side effects (fig. S7, A and B, and table S1). Correspondingly, the treatment of SNT/Dox resulted in half mice alive after 10 weeks, while the mice in other groups gradually died within 8 weeks (fig. S7C). To further confirm the therapeutic efficacies, immunohistochemical studies of tumor sections were performed with the indicator of Ki-67 and TUNEL staining. As shown in Fig. 6 (B and C), the proliferous cells gradually decreased and the apoptotic cells accordingly increased in the sequence of PBS, Dox, CLNT/Dox, LNT/Dox, CSNT/Dox, CNS/Dox, NS/Dox, SNT/Dox, which again confirmed the satisfactory performance of SNT/Dox. Considering the metastatic nature of breast cancer, we continued to evaluate the antimetastatic performance of these formulations. Compared with other types of nanocarriers, the lung and tibia of tumor-bearing mice treated with SNT/Dox showed the fewest metastases (Fig. 6, D and E). These results thus, together, strengthened our confidence of aforementioned physical activity relationship, which may provide guidance for the rational design of anticancer nanocarriers.

Evaluation of applicability of prediction model on HeLa-xenografted mouse model

Encouraged by the consistence of prediction value and experimental value in breast cancer 4T1 tumor model, we further testified the applicability of this prediction model to other tumor type. To this end, we first used RAW 264.7 cells, HeLa tumor cells, and HeLa MCTS to investigate the time/dose-dependent uptake kinetics of macrophage, time/dose-dependent uptake kinetics of cancer cells, and intratumoral invasion on MCTS, respectively (fig. S8, A to C). Accordingly, we obtained the three parameters (α, k, and D) (fig. S9, A to D), which enabled us to predict the prediction value in vivo. As shown in Fig. 7A, compared to other counterparts, SNT was still predicted to have the most efficient prediction value in vivo due to the strongest intratumoral invasion and a relative longer circulation time (Fig. 3C and fig. S8C), while CLNT with the poorest tumor invasion and the shortest circulation time resulted in the most unsatisfied accumulation in prediction.

For the experiment of tumor accumulation in vivo, we injected DiR (1,1'-dioctadecyl-3,3,3',3'-tetramethylindotricarbocyanine iodide)-labeled nanocarriers and performed fluorescence imaging analysis on HeLa tumor–bearing mice. Among the six types of nanocarriers, SNT exhibited the most pronounced accumulation at tumor site
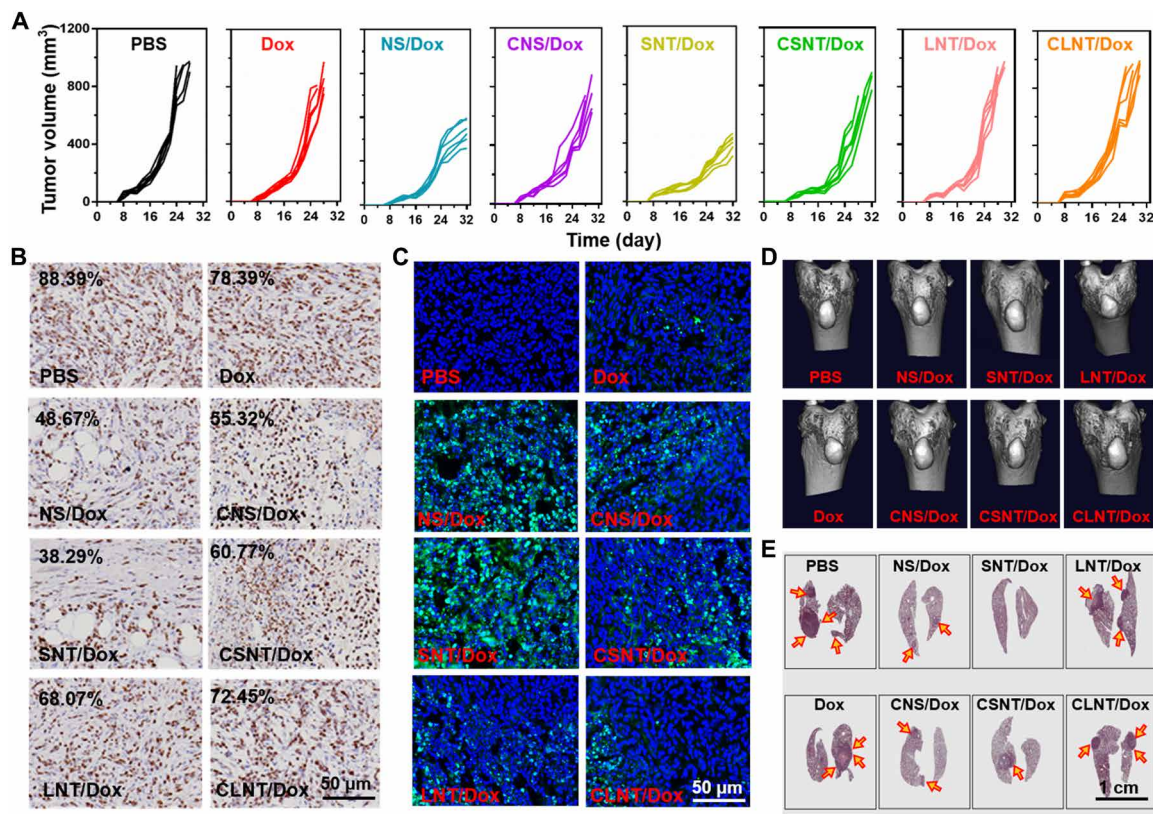
Fig. 6. Comparative evaluation of anticancer efficacy for various nanocarriers/Dox in vivo. (**A**) Growth inhibition curve of 4T1 tumor after treating nanocarriers/Dox formulations with equal Dox concentration during 32 days after injection. (**B**) Representative cell proliferation analysis of tumor tissue by Ki-67 method. (**C**) Representative cell apoptosis of tumor tissue by the TUNEL method. (**D**) Bone metastasis at homolateral by computed tomography scanning. (**E**) Hematoxylin and eosin (H&E) staining images of collected lung tissues. The lung metastasis nodules are indicated by the yellow arrows.

compared to other counterparts (Fig. 7B), which was consistent with the prediction results. More specifically, both experimental value and the prediction value decreased in the same sequence of SNT, NS, CNS, LNT, CSNT, and CLNT (Fig. 7C), again demonstrating that the prediction model is also applicable to HeLa tumor type. Note that the sequence of delivery efficiency between CSNT and LNT showed a tiny difference on HeLa and 4T1 models. However, this was acceptable since these two tumors had different cancer cells for uptake and different extracellular matrices for penetration. In addition, we carried out in vivo antitumor experiments of these nanocarriers/Dox on HeLa-xenografted model. As shown in Fig. 7D, SNT/Dox had the most superior antitumor performance compared with other counterparts. All these results together supported that our prediction model could be used to comparatively predict the nanocarriers' accumulation performance at the tumor site and further therapeutic efficiency in vivo.

DISCUSSION

In summary, it bears emphasis that our experimental data and simulations each revealed the preferred physical properties for each of the delivery stages from blood circulation through to cancer uptake, and our models help to understand these findings. During the blood circulation, spherical shape, low rigidity, and small size could improve the stealth effect to macrophage. Once it transmigrated into solid tumor, tubular shape, low rigidity, and small size became the

optimized physical properties for intratumoral invasion. With the integration of these steps, SNT lastly achieved the most efficient delivery performance over other counterparts, leading to the most potent inhibition on the tumor development and metastasis. We believe this physico-activity relationship offered guidance for the rational design of nanocarriers.

In addition to the blood circulation and intratumoral invasion, the stage of nanocarriers across tumor vessels is also a key factor during the passive targeting process. Several mechanisms of nanocarriers crossing the tumor vessels have been reported. Classically, nanocarriers accumulated at tumor site due to the enhanced permeability and retention effect, which enabled nanoparticles to extravasate through the defect of blood vessel wall. Much differently, Chan and co-workers (37) made an important finding that nanoparticles could use active transport through transendothelial pathways to enter solid tumors. In another recent study, Leong and co-workers (38) found an interesting mechanism that the nanoparticles per se could lead to the formation of micrometer-sized gaps in the blood vessel endothelial walls through disruption of the vascular endothelial (VE)–cadherin-VE-cadherin homophilic interactions at the adherens junction, which revealed a feasible self-reinforced manner for well accumulation in the tumor. Once the mechanism of crossing the tumor vessel is clear and the capacity can be accurately evaluated in vitro, the parameter for this process can be obtained for further incorporating into the prediction function formula. Similarly, this model can also
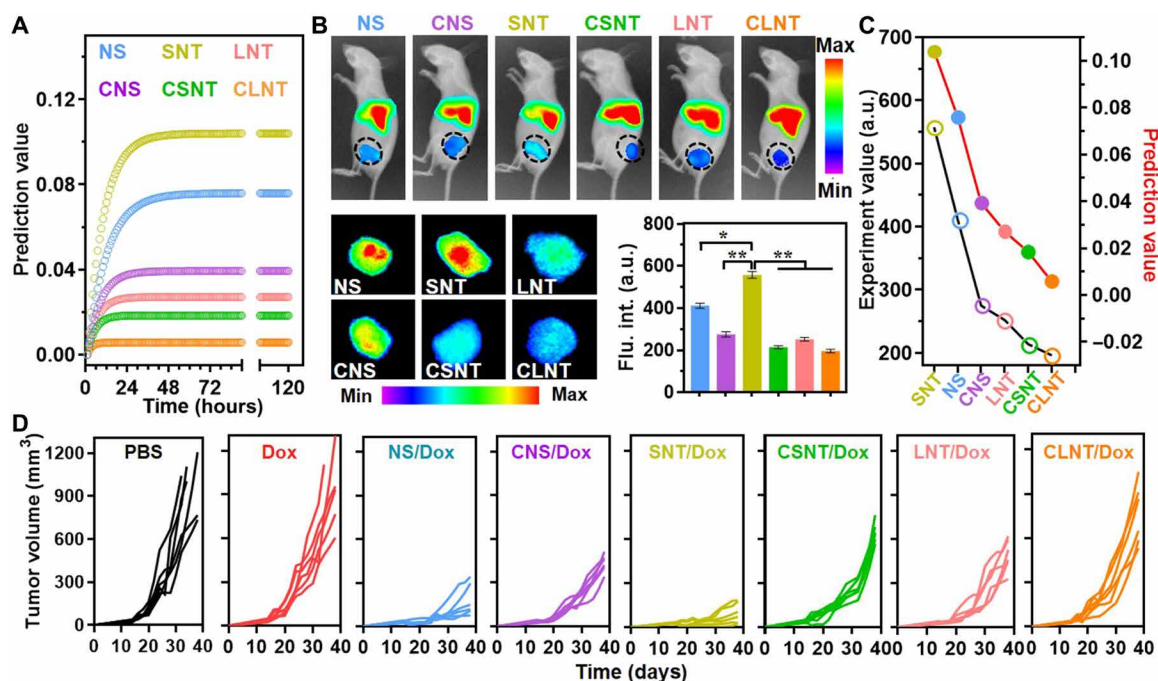
Fig. 7. The evaluation of applicability of prediction model on HeLa-xenografted mouse model. (**A**) The prediction value of various nanocarriers in the HeLa tumor over time. (**B**) In vivo imaging of biodistribution of nanocarriers in HeLa tumor–bearing mice after 120 hours and ex vivo fluorescence imaging of tumors of different nanocarriers and corresponding quantitative analysis. (**C**) Sequence of prediction value and experimental value at HeLa tumor site in vivo with different nanocarriers. The experimental value and the prediction value at tumor sites showed the same order. Solid dots indicate the prediction values, and hollow dots indicate experiment value. (**D**) Growth inhibition curve of HeLa tumor with various nanocarriers/Dox during 40 days. Data in (B) and (D) represent the means ± SD ($n = 6$). Statistical significance between multiple groups was calculated using one-way ANOVA for (B). $*P < 0.05$ and $**P < 0.01$.

be used to predict more sequential and complexed anticancer delivery progress, such as the incorporation of intracellular trafficking and responsive release, with the addition of corresponding parameters. Moreover, our prediction function formula may be incorporated with the specific parameters that represented the patient-specific microenvironments for guiding nanocarrier optimal design and further personalized therapy (*39*).

It was important to emphasize that one focus of our study was the comparative investigation of delivery performance of six nanocarrier types with systematically altered physical properties including size, shape, and rigidity, rather than identifying an optimal one-size-fits-all nanocarrier for the anticancer delivery field. Meanwhile, we anticipated that other nanocarrier types could have outperformed the SNT if they were further designed with positive charge and/or target ligand. At minimum, it is clear that we now have a prediction model that can use three in vitro parameters (α, k, and D) to comparatively predict the nanocarriers' accumulation at the tumor site for in vivo delivery performance.

More generally, our work opened the avenue for the utility of theoretical models for informing design choices for nanocarriers. In addition to physical properties of size, shape, and rigidity, these theoretical models are also applicable for nanocarriers with other physicochemical properties. Similarly, further modification and arrangement of these models in alternative or more highly elaborated pipelines can further help researchers design nanocarriers for a variety of other medical applications. They can be expected to present previously unavailable flexibility and design space for prototyping early particle designs, without the need for extensive in vivo testing.

MATERIALS AND METHODS
Materials
α-Lac, Dox (99.5%), triethylamine (99.5%), glutaraldehyde (25%), anhydrous calcium chloride (CaCl$_2$; 99.5%), and tris(hydroxymethyl) aminomethane were purchased from Sigma-Aldrich (USA). The fluorescent hydrophobic dyes Cy5 and DiR were purchased from Fanbo Biochemical Co. (Beijing, China). *Bacillus licheniformis* protease (BLP) was a gift from Novozymes, Denmark. The mouse breast cancer cells (4T1) human cervical cancer cell line (HeLa cells), mouse leukemia cells of monocyte macrophage (RAW 264.7 cells), and mouse macrophage cells (J774A.1 cells) were purchased from the Cell Resource Center (Peking Union Medical College Headquarters of National Infrastructure of Cell Line Resource). Primary macrophages were extracted from mouse abdominal cavity according to the literature method. Balb/c mice were obtained from Vital River Laboratories (Beijing, China).

Preparation of nanocarriers
First, α-lac (30 g/liter) dissolved in 75 mM tris-HCl buffer (pH 7.4) was partially hydrolyzed by BLP (BLP–to–α-lac weight ratio, 1:25) at 50°C for 30 min. The hydrolyzed amphiphilic peptides were self-assembled into NSs by a water ultrasound for 30 s (*40*). The LNTs were synthesized by adding Ca^{2+} (Ca^{2+}–to–α-lac weight ratio, 1:63) to above hydrolysis system and by prolonging the reaction to 60 min. The SNT was obtained by ultrasonically breaking of the LNT. Subsequently, after differential centrifugation (10,000 rpm for 10 min), the uniform SNT was obtained in precipitation. The cross-linked nanocarriers of CLNT, CSNT, and CNS were prepared by cross-linking

LNT, SNT, and NS with 2.5% glutaraldehyde (glutaraldehyde–to–α-lac weight ratio, 1:3; α-lac, 3 g/liter).

Preparation of six Dox-loaded nanocarriers

Two milligrams of Dox was dissolved in 2 ml of dichloromethane, and 1.43 μl of trimethylamine was added to desalt the hydrophilic Dox into hydrophobic form. The reaction was carried out overnight for fully desalinization. Then, the hydrophobic anticancer drug Dox could be loaded in those nanocarriers by simply mixing Dox (dissolved in ethanol, 1 mg/ml) with nanocarriers' buffer solution (pH 7.5) at a volume ratio of 1:10 under the vertical rotation overnight. Last, nanocarriers/Dox were collected after freeze-drying. To facilitate the subsequent fluorescent imaging and measurement, lipophilic dyes Cy5 and DIR were loaded in nanocarriers instead of Dox using the same process.

Drug-loading efficiency

The ultraviolet absorbance of Dox at 480 nm with gradient concentrations was measured by a multifunction microplate reader (Infinite M200, Tecan) to draw the absorbance-concentration standard curve. The drug-loading (DL) efficiency of nanocarriers/Dox was determined as follows. Briefly, lyophilized nanocarriers/Dox were dissolved in 0.1 ml of alcohol. The absorbance of the solution at 480 nm was measured with the multifunction microplate reader, and the amount of Dox was determined according to the standard curve. The DL efficiency of nanocarriers/Dox was calculated according to Eq. 1

$$DL\% = \frac{drug_{weight}}{nanocarriers_{weight} + drug_{weight}} \times 100\% \quad (1)$$

TEM characterization of nanocarriers

The uranium acetate–stained samples were dropped on the copper grid for three replicates. The morphology of the nanocarriers was observed by TEM at 80 kV (JEM-1400, JEOL).

AFM characterization of nanocarriers

The samples were added to the clean mica plate and dried with ear washing bulb for three replicates. The rigidity of nanocarriers was measured by AFM (FastScan Bio, Bruker). Fifty force curves were collected for each type of various nanocarriers, and the representative retract curves were used to fit the Young's modulus.

Colloidal stability of nanocarriers

The dispersible stability of different nanocarriers in cell culture media (pH 7.4) was evaluated by analyzing its size distribution and zeta potential by dynamic light scattering (Nano-ZS 90, Malvern) at 25°C for seven consecutive days. In general, nanocarriers/Dox solution was prepared in PBS buffer at a concentration of 0.5 mg/ml (protein concentration) and incubated at 37°C in cell culture media. One milliliter of the solution was collected for size distribution and zeta potential measurement.

The qualitative evaluation of cellular uptake by CLSM

The cellular uptakes of different Cy5 [excitation (Ex) wavelength, 640 nm; emission (Em) wavelength, 670 nm]–labeled nanocarriers (nanocarriers/Cy5, Dox was replaced by Cy5 in the nanocarriers) were observed by CLSM (SP5, Leica). After being seeded in the coverglass-bottom dishes and incubated for 24 hours, J774A.1 macrophages or 4T1 cells were cultured with nanocarriers/Cy5 (red) at a protein con-

centration of 100 μg/ml for another 12 hours. Subsequently, the cells were fixed by 4% formaldehyde after washing away the adhered nanocarriers. Before observing the corresponding fluorescence images of the cells by UltraVIEW (PerkinElmer, America), the cell membrane was labeled by Alexa Fluor 488–phalloidin (green; Ex wavelength, 488 nm; Em wavelength, 520 nm), and the cell nucleus was labeled by Hoechst 33342 (blue; Ex wavelength, 346 nm; Em wavelength, 460 nm).

The qualitative evaluation of cellular uptake by FCM

FCM (Beckman Coulter) was also used to study the cellular endocytic dynamics of different nanocarriers. 4T1 cells, J774A.1 cells, HeLa cells, RAW 264.7 cells, and primary macrophages were seeded in 24-well plate and incubated for 24 hours to allow cell attachment. The cells were cultured with different concentrations of nanocarriers/Cy5 (10, 20, 30, 40, 50, 60, 70, 80, 90, and 100 μg/ml) for different times (0.5, 1, 2, 4, 8, 12, 24, 30, and 36 hours). Subsequently, cells were washed with PBS, and the uptake amount of nanocarriers/Cy5 was determined by FCM. Data were obtained by collecting 10,000 cells for each sample.

CCK-8 cytotoxicity assay for nanocarriers

The cytotoxicity was determined using the CCK-8 (Beyotime, China) assay. Briefly, 4T1 or other cells (HeLa cells, J774A.1 cells, RAW 264.7 cells, HUVECs, and mouse primary macrophages) were seeded in 96-well plate at a density of 1.5×10^4 cells and incubated for 24 hours to allow cell attachment. Then, the cells were cultured with different nanocarrier formulations (equivalent protein concentration ranged from 0 to 100 μg/ml) and corresponding additives for 24, 48, and 72 hours. CCK-8 test solution was added to each well of the plate (the volume of the CCK-8 test solution in each well is $^1/_{10}$ of the total volume) and incubated for another 3 hours. After selective reduction by viable cells, the absorption intensity of each well at 450 nm was measured. Percentage of the viability was normalized according to the untreated cells.

In vitro tumor penetration of nanocarriers

4T1 cells or HeLa cells suspended in RPMI 1640 culture medium were seeded onto agarose (Sigma-Aldrich, Shanghai, China)–precoated 96-well plates at a density of 2000 cells per well to grow the MCTSs. MCTSs were grown for 4 days until they reached 500 μm in diameter before use. Different nanocarriers/Cy5 formulations (protein concentration of 100 μg/ml) were added into the pores in 96-well plates and cultured for different times (1, 6, 12, 24, 36, and 48 hours). Next, the MCTSs were removed and collected using a pipette. Then, these MCTSs were gently washed three times with cold PBS. The penetration of different Cy5-labeled nanocarriers was observed by CLSM (SP5, Leica).

In vitro growth inhibition of MCTS by nanocarriers/Dox

MCTSs were cultured with Dox (10 μg/ml) and nanocarriers/Dox formulations (equivalent Dox concentration of 10 μg/ml) for 72 hours. After fixed in 4% paraformaldehyde, the MCTSs were cut into 20-μm-thick slices with a microtome. TUNEL assay was performed according to the instructions of the in situ cell death detection kit (Merck Millipore, Darmstadt, Germany). Dox (10 μg/ml) and nanocarriers/Dox formulations (equivalent Dox concentration of 10 μg/ml) were administered to MCTS every 3 days. The morphology and the variation of the MCTS shapes were monitored by capturing the images

using a light microscope, and the diameters (d) were measured. Assuming the MCTS as spheres, the volume was calculated according to the formula as follows

$$V = 4/3 \times \pi \times (d/2)^3 \qquad (2)$$

The data were reported as the mean volume of three spheroids ± SD.

In vivo tumor targeting evaluation of nanocarriers

4T1-xenografted mouse model of mammary adenocarcinoma was established by injecting 1×10^6 4T1 cells (suspended in 100 µl of PBS buffer) into the ventral mammary fat pad of the female Balb/c mice. HeLa tumor–bearing mice were established by injecting 1×10^8 HeLa cells (suspended in 100 µl of PBS buffer) into subcutaneous. To observe the biodistribution of different nanocarrier formulations in vivo, Dox was replaced by fluorescent hydrophobic dye DIR (Ex wavelength, 748 nm; Em wavelength, 780 nm). Nanocarriers/DiR (100 µl) with a protein concentration of 100 µg/ml were intravenously injected to 4T1 tumor–bearing female Balb/c, and their biodistribution were observed using an in vivo imaging system (FX Pro, Kodak) at various time intervals of 1, 4, 24, 36, 48, and 120 hours. After the last imaging at 120 hours, tumors and organs of interest were excised and imaged to observe the fluorescence distribution.

In vivo pharmacokinetic evaluation of nanocarriers

To study the pharmacokinetic behavior of different nanocarriers in vivo, Balb/c mice were divided into six groups ($n = 3$), and nanocarriers/Cy5 were intravenously injected at a protein concentration of 100 µg/ml. Whole-blood samples were collected from the orbit at predestined time intervals (0.5, 1, 2, 4, 6, 8, 12, and 24 hours) using a heparinized tube. All the blood samples were centrifuged at 4000g for 10 min at 4°C. The fluorescence intensity of equal serum volume was measured by an automatic microplate reader (Infinite M200, Tecan). Relative fluorescence intensity was normalized according to the untreated mice.

In vivo anticancer efficacy evaluation

To compare the antitumor effect of the Dox-loaded nanocarriers, 4T1-xenografted mice or HeLa tumor–bearing mice were randomly divided into eight groups (each group, $n = 6$). The treatments were started when the average tumor volume reached approximately 100 mm^3 by intravenously administering with PBS, Dox, LNT/Dox, CLNT/Dox, SNT/Dox, CSNT/Dox, NS/Dox, and CNS/Dox (equivalent Dox concentration, 0.5 mg/ml; 200 µl for each mouse) once every other day until day 32. The longest and shortest tumor diameters (in millimeters) were measured. In addition, after the last treatment at day 32, the number of surviving mice in each group was monitored, and the survival curve was obtained. Tumor volumes were calculated by

$$V = \frac{L \times W^2}{2} \qquad (3)$$

where L is the longest tumor diameter and W is the shortest tumor diameter (in millimeters).

Immunohistochemical section evaluations of nanocarriers

One week after the completion administering nanocarriers/Dox, one mouse was taken from each group for immunofluorescence analysis. A TUNEL apoptosis detection kit was used for nucleus apoptosis of tumor tissues, and a proliferating cell nuclear antigen–Ki-67 was used for nucleus proliferation of tumor tissue.

Antimetastasis effect evaluations of nanocarriers

4T1 mammary adenocarcinoma is highly tumorigenic and invasive and can spontaneously metastasize from the primary mammary gland to distant sites, including the lungs and bone tissues. To evaluate the antimetastasis effect of different Dox-loaded nanocarriers in vivo, the bone erosion at homolateral tibia caused by tumor metastasis of above mice in each group was imaged using a micro–computed tomography scanner (Quantum FX, Caliper Life Sciences). Lung metastasis in different treatment groups was evaluated by hematoxylin and eosin (H&E) staining.

Safety evaluation of Dox-loaded nanocarriers anticancer therapy

To further evaluate the safety of different formulations in vivo, the body weight of mice in each group was recorded. In addition, the serum levels of urea nitrogen, lactate dehydrogenase, alanine aminotransferase, aspartate transaminase, and alkaline phosphatase were analyzed using an automated analyzer (Hitachi-917, Hitachi Ltd., Japan). The organs (heart, liver, spleen, lung, and kidney) from mice of each group were sliced and stained by H&E staining.

Safety evaluation of naked nanocarriers in healthy mice

For confirming the safety of various naked nanocarriers in vivo, the main organs and blood of the mouse were taken out for corresponding analyses (including H&E-stained tissue sections, serum biochemical parameters, and blood routine examination). Specifically, the indicators of blood routine (white blood cell, red blood cell, hematocrit, hemoglobin, mean corpuscular hemoglobin, mean corpuscular hemoglobin concentration, mean corpuscular volume, and plateletocrit) were detected by blood routine analyzer (MEK-7222K, Japan).

Animal care

Balb/c mice or Balb/c-nu mice, 4 to 6 weeks of age, were obtained from Vital River Laboratories (Beijing, China). This study was performed in strict accordance with the Regulations for the Care and Use of Laboratory Animals and Guideline for Ethical Review of Animal (China, GB/T 35892-2018). All animal experiments were reviewed and approved by the Animal Ethics Committee of the Institute of Process Engineering (approval ID: IPEAECA2017126).

Molecular dynamics simulations

Similar to our previous work, the coarse-grained simulation system for investigating the diffusivity of the nanocarriers in tumor extracellular matrix comprised an irregular polymer network and dozens of nanocarriers (*22*, *34*). The polymer network was used to represent the protein (the most abundant protein is collagen) fibers with an average mesh size of 8σ (where σ is the unit of the length in our simulation), as shown in fig. S4 (A and B). The nanocarrier with different shapes, lengths, and stiffnesses was modeled as a single bead (NS and CNS) or a linear chain model with different chain lengths (tubular nanocarriers) (fig. S4D). To keep the integrity of the polymer network and NTs during the simulation, the adjacent beads in NTs and in network were connected via the harmonic bond potential.

$$U_b = \frac{1}{2}k_b(r - r_0)^2 \qquad (4)$$

where spring constant $k_b = 50 k_B T / \sigma_d^2$ and the equilibrium bond length $r_0 = 1.0 \sigma_d$. The harmonic angle potential was adopted for tuning the rigidities of the network and NTs

$$U_a = \frac{1}{2} k_a (\theta - \theta_0)^2 \tag{5}$$

where the equilibrium angle $\theta = \pi$ and the spring constant $k_a = 50 k_B T / \text{rad}^2$ for the network. We set $k_a = 500 k_B T / \text{rad}^2$ for CSNT and CLNT and $k_a = 5 k_B T / \text{rad}^2$ for SNT and LNT, to reflect their different rigidities. The cross-linked network beads were restrained via fixing the positions of beads using self-harmonic spring potential with the spring constant $k_s = 20 k_B T / \sigma^2$. The CNS and NS were represented using single CG (coarse-grained) beads. We adopted a modified Lennard-Jones (LJ) potential with soft core, to tune the rigidity of NS

$$U_{sLJ} = \lambda^n 4 \in \left\{ \frac{1}{\left[a(1-\lambda)^2 + \left(\frac{r}{b_d} \right)^6 \right]^2} - \frac{1}{a(1-\lambda)^2 + \left(\frac{r}{b_d} \right)^6} \right\} \tag{6}$$

where λ is an activation parameter, if $\lambda = 1$ the potential would be identical as standard LJ potential. We set $\lambda = 0.5$, $\alpha = 0.5$, and $n = 2$ for the soft repulsive LJ potential, to represent the NS. The CNS was modeled via standard LJ potential. We set the parameter b between the (C)NS and beads in network to $3.25 \sigma_d$ and same interaction parameters as tubular model. The nonbonded affinity between nanocarriers beads and polymer network beads in the system was described using the LJ potential

$$U_{LJ} = 4 \alpha_k \left[\left(\frac{b_d}{r} \right)^{12} - \left(\frac{b_d}{r} \right)^6 \right] \tag{7}$$

where α_k is the interaction parameter and we set it as $0.1 k_B T$; b_d is the distance where the LJ potential equals to 0, and we set b_d between beads in NTs and in network as $2 \sigma_d$ and $1 \sigma_d$ for other combinations. The cutoff radius $r_{cut} = 2.5 b_d$, beyond which the LJ potential was 0.

In each simulation, there were 120 (C)SNTs or 40 (C)LNTs contained in the system, to guarantee that they occupied the same volume fraction. The box length in each dimension was σ_d with periodic boundary conditions applied in all the three dimensions, and the simulations were performed under NVT ensemble. During the simulations, we recorded the center of mass (COM) of each nanocarriers every $10 \tau_d$ (τ_d is the unit of the time in our simulation), and then the MSD and effective diffusivities were calculated using the following equations

$$\text{MSD}(t) = \langle (x_t - x_0)^2 + (y_t - y_0)^2 + (z_t - z_0)^2 \rangle \tag{8}$$

where x, y, and z represent the COM of the nanocarriers, t is the duration of the time lag, and $\langle \cdots \rangle$ represents the average of all the nanocarriers. The velocity Verlet algorithm was used to perform time integration during the simulations. The total simulation time was $1 \times 10^8 \tau_d$. After about $5 \times 10^5 \tau_d$ relaxation, the MSD calculations were started.

The CGMD simulations for the uptake of the nanocarrier are based on the one-particle-thick CG model developed by Yuan et al (33). This highly coarse-grained lipid model can reproduce the correct mechanical properties of biological membranes and capture the essential features of nanocarrier uptake within reasonable temporal and spatial scales. Briefly, the membrane comprised a mixture of

binding agent/lipid, and the density of the agent is $0.004/\sigma^2$, which is on the same order of magnitude as the binding agent protein density in real cell membrane (41). Each lipid or binding agent molecule is represented by one bead, as shown in fig. S4H. Following the notation from the original paper, the interparticle interaction between each pair of nanocarrier beads was described by a combination of two functions, $u(r)$ and $\phi(\hat{\mathbf{r}}_{ij}, \mathbf{n}_i, \mathbf{n}_j)$, which represented the distance and orientation dependences, respectively, as follows

$$U(\mathbf{r}_{ij}, \mathbf{n}_i, \mathbf{n}_j) = \begin{cases} u_R(r) + \varepsilon_{\text{beads-beads}} [1 - \phi(\hat{\mathbf{r}}_{ij}, \mathbf{n}_i, \mathbf{n}_j)] & r < r_{\min} \\ u_A(r) \phi(\hat{\mathbf{r}}_{ij}, \mathbf{n}_i, \mathbf{n}_j) & r_{\min} < r < r_c \end{cases} \tag{9}$$

where

$$u_A(r) = -\varepsilon_{\text{beads-beads}} \cos^{2\zeta} \left(\frac{\pi}{2} \frac{r - r_{\min}}{r_c - r_{\min}} \right) \quad r_{\min} < r < r_c \tag{10}$$

$$u_R(r) = \varepsilon_{\text{beads-beads}} \left[\left(\frac{r_{\min}}{r} \right)^4 - 2 \left(\frac{r_{\min}}{r} \right)^2 \right] r < r_{\min} \tag{11}$$

$$\phi(\hat{\mathbf{r}}_{ij}, \mathbf{n}_i, \mathbf{n}_j) = 1 + \mu(a(\hat{\mathbf{r}}_{ij}, \mathbf{n}_i, \mathbf{n}_j) - 1) \tag{12}$$

$$a(\hat{\mathbf{r}}_{ij}, \mathbf{n}_i, \mathbf{n}_j) = (\mathbf{n}_i \times \hat{\mathbf{r}}_{ij}) \cdot (\mathbf{n}_j \times \hat{\mathbf{r}}_{ij}) + \sin \theta_0 (\mathbf{n}_i, \mathbf{n}_j) \cdot \hat{\mathbf{r}}_{ij} - \sin^2 \theta_0 \tag{13}$$

In these equations, $\mathbf{r}_i$ and $\mathbf{r}_j$ represented the center position vectors of beads i and j, $\mathbf{r}_{ij} = \mathbf{r}_i - \mathbf{r}_j$, $r = \|\mathbf{r}_{ij}\|$, and $\hat{\mathbf{r}}_{ij} = \mathbf{r}_i / r$. The unit vectors $\mathbf{n}_i$ and $\mathbf{n}_j$ represented the axes of symmetry of the beads i and j, respectively. In the simulations, we chose the same parameters $\varepsilon_{\text{beads-beads}} = 1\varepsilon$, $\xi = 4$, and $r_c = 2.6\sigma$ as used in the original paper. The other two parameters (μ and $\sin\theta_0$) were used to modify the bending rigidity of the membrane, which are taken as $\mu = 3$ and $\sin \theta_0 = 0$ in our simulations as used similar to Shen et al. (42). The models of each different type of NTs are used similar to above model, i.e., a linear CG chains with different rigidities and lengths. The CNS and NS were constructed by placing 64 particles on a spherical surface of radii 2.0σ in optimal spherical coverings. The LJ potential and Weeks-Chandler-Anderson (WCA) potential were used as follows to describe the nonbonded interactions between nanocarriers and cellular membrane

$$V(r_{ij}) = 4 \varepsilon_{ij} \left[\left(\frac{b}{r_{ij}} \right)^{12} - \left(\frac{b}{r_{ij}} \right)^6 \right] r_{ij} < r_{cut} \tag{14}$$

$$V_{\text{WCA}}(r_{ij}) = 4 \varepsilon_{ij} \left[\left(\frac{b}{r_{ij}} \right)^{12} - \left(\frac{b}{r_{ij}} \right)^6 + 0.25 \right] \quad r_{ij} < r_{cut} = 2 \tag{15}$$

where ε_{ij} is the depth of the energy well, b is the equilibrium length between two beads, and r_{cut} is the cutoff distance. The interaction parameters are listed in table S1. In the simulation, to avoid the distribution of the nanocarriers to the equilibrium state of the membrane, a long-time (about $5 \times 10^5 \tau$) equilibrium simulation was performed before the uptake process in the initial stage. Then, a nanocarrier was put near the surface of the membrane and performed a long-time simulation to investigate the kinetics of the nanocarrier uptake. The velocity-Verlet algorithm was used to perform the time integration. The time step in the CGMD simulations is set to be 0.01τ. A Langevin thermostat was used to control the system temperature at $k_B T = 0.2\varepsilon$. To maintain a constant binding agent density in the remote region of the membrane during the simulation processes, a

special region is used to monitor the density of the binding agent. Once the density of the binding agent is lower than a threshold (0.004) in the monitor region, a random lipid agent is converted to a binding agent in this region whenever a ligand-binding agent binding event occurs. In all above simulations, the periodic boundary condition applied three directions, and all the simulations were performed using the LAMMPS code.

Theoretical model
The diffusion of nanocarriers in the tumor
The distribution of nanocarriers within the interstitial space of a spheroid segment of radius R can be described as

$$\frac{\partial C}{\partial t} = \frac{D}{r^2}\frac{\partial}{\partial r}\left(r^2\frac{\partial C}{\partial r}\right) \quad 0 < r < R, t > 0 \tag{16}$$

where C is the concentration of nanocarriers and D is the diffusion coefficient of the nanocarriers in the interstitial space of the spherical tumor with radius of R. At the interface of the surrounding medium with the spheroid, the nanocarriers' concentration is continuous with the interstitial fluid of the spheroid

$$C(R,t) = C_0 \quad t \geq 0 \tag{17}$$

where C_0 is the concentration of nanocarriers in the surrounding medium. After a bolus injection of Tobacco mosaic virus into the surrounding medium, C_0 equals the ratio of the mass of the nanocarriers to the volume of the surrounding medium. At the center of the spheroid, by spherical symmetry, there is no net diffusion flux so that the concentration gradient is zero

$$\frac{\partial C}{\partial r} = 0 \quad r = 0 \; t \geq 0 \tag{18}$$

Initially, there are no nanocarriers in the interstitial space of the spheroid

$$C(r,0) = 0 \quad 0 < r < R \tag{19}$$

Above all, the math equations for describing the distribution of nanocarriers in the spheroid were as follows

$$\begin{cases} \dfrac{\partial C}{\partial t} = \dfrac{D_M}{r^2}\dfrac{\partial}{\partial r}\left(r^2\dfrac{\partial C}{\partial r}\right) & 0 < r < R, t > 0 \\ C(r,0) = 0 & 0 < r < R \\ C(R,t) = C_0 & t \geq 0 \\ \dfrac{\partial C}{\partial r} = 0 & r = 0 \; t \geq 0 \end{cases} \tag{20}$$

The solution of these equations is

$$\frac{C(r,t)}{C_0} = 1 - 2R\sum_{n=1}^{\infty}\frac{(-1)^{n+1}}{n\pi r}\cdot\sin\left(\frac{n\pi r}{R}\right)\cdot e^{-(n\pi)^2\cdot\frac{D_M t}{R^2}} \tag{21}$$

In our MCTSs model, the solid tumor comprised the cancer cell with a fraction of 91.9% and tumor matrix (8.1%). Thus, the nanocarriers would be taken up by the cell when they meet the cell membrane during the penetration, and the mathematical model for describing the concentration distribution of the nanocarriers in the inner of the spheroid should be modified as

$$\begin{cases} \dfrac{\partial C_u}{\partial t} = \dfrac{D_u}{r^2}\dfrac{\partial}{\partial r}\left(r^2\dfrac{\partial C_u}{\partial r}\right) - kC_u & 0 < r < R, t > 0 \\ C_u(r,0) = 0 & 0 < r < R \\ C_u(R,t) = C_0 & t \geq 0 \\ \dfrac{\partial C_u}{\partial r} = 0 & r = 0 \; t \geq 0 \end{cases} \tag{22}$$

where C_u and D_u are the concentration and diffusion coefficient of nanocarriers in the interstitial space of the spherical tumor with radius of R, respectively, and k is the constant rate at which nanocarrier is irreversibly taken up by cells. In this case, the solution becomes

$$\frac{C_u(r,t)}{C_0} = 1 - 2R\sum_{n=1}^{\infty}\frac{(-1)^{n+1}}{n\pi r}\cdot\sin\left(\frac{n\pi r}{R}\right)\cdot\frac{k + D_u\frac{(n\pi)^2}{R^2}\cdot e^{-\left(k+D_u\frac{(n\pi)^2}{R^2}\right)t}}{k + D_u\frac{(n\pi)^2}{R^2}} \tag{23}$$

Last, the total amount of diffusing nanocarriers that entered the spheroid at time t can be predicted by integrating the nanocarrier concentration over the whole-spheroid volume

$$M_1(t) = \int_{r=0}^{R}\frac{C(r,t)}{C_0}\,dr = \frac{4}{3}\pi R^3 C_0\left[1 - \frac{6}{\pi^2}\sum_{n=1}^{\infty}\frac{1}{n^2}e^{-(n\pi)^2\frac{2D_M t}{R^2}}\right] \tag{24}$$

$$M_2(t) = \int_{r=0}^{R}\frac{C_u(r,t)}{C_0}\,dr = \frac{4}{3}\pi R^3 C_0\left[1 - \frac{6}{\pi^2}\sum_{n=1}^{\infty}\frac{1}{n^2}\frac{k + D_u\frac{(n\pi)^2}{R^2}\cdot e^{-\left(k+D_u\frac{(n\pi)^2}{R^2}\right)t}}{k + D_u\frac{(n\pi)^2}{R^2}}\right] \tag{25}$$

$$\text{Prediction value} = \phi M_1(t) + (1-\phi)M_2(t) \tag{26}$$

where M_1 and M_2 are the total amount of nanocarriers in the inner of the spheroid without and with cellular uptake, respectively, and ϕ is the component fraction of the tumor matrix and set as $\phi = 8.1\%$ in this work. Once we know the model parameter (D_M, D_U, and k), we can predict the distribution of the nanocarriers concentration within the tumor varied with the position and time.

The blood circulation of the nanocarriers
The blood circulation of the nanocarrier was described by the first-order decay pharmacokinetics model, i.e., the attenuation of the nanocarriers in the blood keeps a constant rate

$$\frac{dC_b(t)}{dt} = -\beta C_b(t) \tag{27}$$

where C_b is the concentration of nanocarriers in the blood. The profile of the nanocarriers in the blood varied with circulation time is similar to

$$C_b(t) = C_i e^{-\beta t} \tag{28}$$

where C_i is the initial injected concentration of the nanocarriers.

The uptake of the macrophage
The previous studies have shown that the different blood circulation performances of the soft and stiff nanocarriers were attributable to their distinct phagocytosis profiles. Moreover, the uptake of the macrophage is an important way to clean the extraneous nanocarriers. In this work, we used a simple equation (43, 44)

$$C_M(t) = C_b(1 - e^{-\alpha t}) \tag{29}$$

where C_M and C_b are the concentration of the nanocarriers in the macrophage and blood, respectively, and α is the rate of the uptake.

Rate of cellular uptake

The rate of cellular uptake of nanocarriers in cancer cells was characterized experimentally, as we all know that the number of particles uptake by the cell would reach a stable value in a short time (about 5 hours). So here, we fit the rate of cellular uptake with an equation using the early-stage experiment data, i.e., data before reach the stable state

$$N(t) = \begin{cases} kt & t < 5 \\ N(5) & t > 5 \end{cases} \quad (30)$$

Once we obtained the uptake rate of each type of nanocarriers, we can fit the diffusion coefficient of each type of nanocarriers in the tumor spheroid.

Statistical analysis

All the data represent the means ± SD. Statistical analysis was performed with Prism 8.0 software (GraphPad Software) by one-way analysis of variance (ANOVA).

SUPPLEMENTARY MATERIALS

Supplementary material for this article is available at http://advances.sciencemag.org/cgi/content/full/7/6/eaba2458/DC1

View/request a protocol for this paper from *Bio-protocol*.

REFERENCES AND NOTES

1. H. Wang, Y. Wu, R. F. Zhao, G. J. Nie, Engineering the assemblies of biomaterial nanocarriers for delivery of multiple theranostic agents with enhanced antitumor efficacy. *Adv. Mater.* **25**, 1616–1622 (2013).
2. L. Liu, C. F. Xu, S. Iqbal, X. Z. Yang, J. Wang, Responsive nanocarriers as an emerging platform for cascaded delivery of nucleic acids to cancer. *Adv. Drug Deliv. Rev.* **115**, 98–114 (2017).
3. T. M. Allen, P. R. Cullis, Liposomal drug delivery systems: From concept to clinical applications. *Adv. Drug Deliv. Rev.* **65**, 36–48 (2013).
4. X. Huang, P. K. Jain, I. H. El-Sayed, M. A. El-Sayed, Gold nanoparticles: Interesting optical properties and recent applications in cancer diagnostics and therapy. *Nanomedicine* **2**, 681–693 (2007).
5. M. Ferrari, Cancer nanotechnology: Opportunities and challenges. *Nat. Rev. Cancer* **5**, 161–171 (2005).
6. H. Chen, Z. J. Gu, H. W. An, C. Y. Chen, J. Chen, R. Cui, S. Q. Chen, W. H. Chen, X. S. Chen, X. Y. Chen, Z. Chen, B. Q. Ding, Q. Dong, Q. Fan, T. Fu, D. Y. Hou, Q. Jiang, H. T. Ke, X. Q. Jiang, G. Liu, S. P. Li, T. Y. Li, Z. Liu, G. J. Nie, M. Ovais, D. W. Pang, N. S. Qiu, Y. Q. Shen, H. Y. Tian, C. Wang, H. Wang, Z. Q. Wang, H. P. Xu, J. F. Xu, X. L. Yang, S. Zhu, X. C. Zheng, X. Z. Zhang, Y. B. Zhao, W. H. Tan, X. Zhang, Y. L. Zhao, Precise nanomedicine for intelligent therapy of cancer. *Sci. China Chem.* **61**, 1503–1552 (2018).
7. Y. F. Wang, L. Liu, X. Xue, X. J. Liang, Nanoparticle-based drug delivery systems: What can they really do in vivo? *F1000Res.* **16**, 681 (2017).
8. D. Rosenblum, N. Joshi, W. Tao, J. M. Karp, D. Peer, Progress and challenges towards targeted delivery of cancer therapeutics. *Nat. Commun.* **9**, 1410 (2018).
9. S. Wilhelm, A. J. Tavares, Q. Dai, S. Ohta, J. Audet, H. F. Dvorak, W. C. W. Chan, Analysis of nanoparticle delivery to tumours. *Nat. Rev. Mater.* **1**, 16014 (2016).
10. D. S. Spencer, A. S. Puranik, N. A. Peppas, Intelligent nanoparticles for advanced drug delivery in cancer treatment. *Curr. Opin. Chem. Eng.* **7**, 84–92 (2015).
11. P. T. Wong, S. K. Choi, Mechanisms of drug release in nanotherapeutic delivery systems. *Chem. Rev.* **115**, 3388–3432 (2015).
12. F. Pi, D. W. Binzel, T. J. Lee, Z. Li, M. Sun, P. Rychahou, H. Li, F. Haque, S. Wang, C. M. Croce, B. Guo, B. M. Evers, P. Guo, Nanoparticle orientation to control RNA loading and ligand display on extracellular vesicles for cancer regression. *Nat. Nanotechnol.* **13**, 82–89 (2018).
13. E. Blanco, H. Shen, M. Ferrari, Principles of nanoparticle design for overcoming biological barriers to drug delivery. *Nat. Biotechnol.* **33**, 941–951 (2015).
14. D. Lombardo, M. A. Kiselev, M. T. Caccamo, Smart nanoparticles for drug delivery application: Development of versatile nanocarrier platforms in biotechnology and nanomedicine. *J. Nanomater.* **2019**, 1–26 (2019).
15. X. Zhang, X. Xu, Y. Li, C. Hu, Z. Zhang, Z. Gu, Virion-like membrane-breaking nanoparticles with tumor-activated cell-and-tissue dual-penetration conquer impermeable cancer. *Adv. Mater.* **30**, e1707240 (2018).
16. W. E. Bao, X. W. Liu, Y. L. Lv, G. H. Lu, F. Li, B. Liu, D. Li, W. Wei, Y. Li, Nanolongan with multiple on-demand conversions for ferroptosis-apoptosis combined anticancer therapy. *ACS Nano* **13**, 260–273 (2019).
17. H.-J. Li, J. Liu, X. J. Du, S. Shen, Y. H. Zhu, X. Wang, X. Ye, S. Nie, J. Wang, Smart superstructures with ultrahigh pH-sensitivity for targeting acidic tumor microenvironment: Instantaneous size switching and improved tumor penetration. *ACS Nano* **10**, 6753–6761 (2016).
18. S. E. A. Gratton, P. A. Ropp, P. D. Pohlhaus, J. C. Luft, V. J. Madden, M. E. Napier, J. M. DeSimone, The effect of particle design on cellular uptake pathways. *Proc. Natl. Acad. Sci. U.S.A.* **105**, 11613–11618 (2008).
19. W. Helfrich, Elastic properties of lipid bilayers: Theory and possible experiments. *Z. Naturforsch. C* **28**, 693–703 (1973).
20. H. Gao, W. Shi, L. B. Freund, Mechanics of receptor-mediated endocytosis. *Proc. Natl. Acad. Sci. U.S.A.* **102**, 9469–9474 (2005).
21. J. Sun, L. Zhang, J. Wang, Q. Feng, D. Liu, Q. Yin, D. Xu, Y. Wei, B. Ding, X. Shi, X. Jiang, Tunable rigidity of (polymeric core)-(lipid shell) nanoparticles for regulated cellular uptake. *Adv. Mater.* **27**, 1402–1407 (2015).
22. M. Yu, L. Xu, F. Tian, Q. Su, N. Zheng, Y. Yang, J. Wang, A. Wang, C. Zhu, S. Guo, X. Zhang, Y. Gan, X. Shi, H. Gao, Rapid transport of deformation-tuned nanoparticles across biological hydrogels and cellular barriers. *Nat. Commun.* **9**, 2607 (2018).
23. R. K. Jain, T. Stylianopoulos, Delivering nanomedicine to solid tumors. *Nat. Rev. Clin. Oncol.* **7**, 653–664 (2010).
24. Y. Geng, P. Dalhaimer, S. S. Cai, R. Tsai, M. Tewari, T. Minko, D. E. Discher, Shape effects of filaments versus spherical particles in flow and drug delivery. *Nat. Nanotechnol.* **2**, 249–255 (2007).
25. M. Müllner, S. J. Dodds, T. H. Nguyen, D. Senyschyn, C. J. Porter, B. J. Boyd, F. Caruso, Size and rigidity of cylindrical polymer brushes dictate long circulating properties in vivo. *ACS Nano* **9**, 1294–1304 (2015).
26. C. Bao, B. Liu, B. Li, J. Chai, L. Zhang, L. Jiao, D. Li, Z. Yu, F. Ren, X. Shi, Y. Li, Enhanced transport of shape and rigidity-tuned α-lactalbumin nanotubes across intestinal mucus and cellular barriers. *Nano Lett.* **2**, 1352–1361 (2020).
27. D. Li, M. X. Shi, C. Bao, W. E. Bao, L. W. Zhang, L. L. Jiao, T. Li, Y. Li, Synergistically enhanced anticancer effect of codelivered curcumin and siPlk1 by stimuli-responsive α-lactalbumin nanospheres. *Nanomedicine* **5**, 595–612 (2019).
28. A. C. Anselmo, S. Mitragotri, Impact of particle elasticity on particle-based drug delivery systems. *Adv. Drug Deliv. Rev.* **108**, 51–67 (2017).
29. B. Ouyang, W. Poon, Y. N. Zhang, Z. P. Lin, B. R. Kingston, A. J. Tavares, Y. W. Zhang, J. Chen, M. S. Valic, A. M. Syed, P. Macmillan, J. Couture-Senécal, G. Zheng, W. C. W. Chan, The dose threshold for nanoparticle tumour delivery. *Nat. Mater.* **19**, 1362–1371 (2020).
30. C. R. Thoma, M. Zimmermann, I. Agarkova, J. M. Kelm, W. Krek, 3D cell culture systems modeling tumor growth determinants in cancer target discovery. *Adv. Drug Deliv. Rev.* **69**, 29–41 (2014).
31. K. Han, S. E. Pierce, A. Li, K. Spees, G. R. Anderson, J. A. Seoane, Y. H. Lo, M. Dubreuil, M. Olivas, R. A. Kamber, M. Wainberg, K. Kostyrko, M. R. Kelly, M. Yousefi, S. W. Simpkins, D. Yao, K. Lee, C. J. Kuo, P. K. Jackson, A. Sweet-Cordero, A. Kundaje, A. J. Gentles, C. Curtis, M. M. Winslow, M. C. Bassik, CRISPR screens in cancer spheroids identify 3D growth-specific vulnerabilities. *Nature* **580**, 136–141 (2020).
32. S. Liu, W. Wei, B. Xie, H. Yue, D. Ni, Y. Bao, G. H. Ma, Z. G. Su, Breaching the hyaluronan barrier with PH20-Fc facilitates intratumoral permeation and enhances antitumor efficiency: A comparative investigation of typical therapeutic agents in different nanoscales. *Adv. Healthc. Mater.* **5**, 2872–2881 (2016).
33. H. Yuan, C. Huang, J. Li, G. Lykotrafitis, S. Zhang, One-particle-thick, solvent-free, coarse-grained model for biological and biomimetic fluid membranes. *Phys. Rev. E* **82**, 011905 (2010).
34. C. Huang, Y. Zhang, H. Yuan, H. Gao, S. Zhang, Role of nanoparticle geometry in endocytosis: Laying down to stand up. *Nano Lett.* **13**, 4546–4550 (2013).
35. M. Yu, J. Wang, Y. Yang, C. Zhu, Q. Su, S. Guo, J. Sun, Y. Gan, X. Shi, H. Gao, Rotation-facilitated rapid transport of nanorods in mucosal tissues. *Nano Lett.* **16**, 7176–7182 (2016).
36. J. Wang, Y. Yang, M. Yu, G. Q. Hu, Y. Gan, H. Gao, X. Shi, Diffusion of rod-like nanoparticles in non-adhesive and adhesive porous polymeric gels. *J. Mech. Phys. Solids* **112**, 431–457 (2018).
37. S. Sindhwani, A. M. Syed, J. Ngai, B. R. Kingston, L. Maiorino, J. Rothschild, P. MacMillan, Y. Zhang, N. U. Rajesh, T. Hoang, J. L. Y. Wu, S. Wilhelm, A. Zilman, S. Gadde, A. Sulaiman, B. Ouyang, Z. Lin, L. Wang, M. Egeblad, W. C. W. Chan, The entry of nanoparticles into solid tumours. *Nat. Mater.* **19**, 566–575 (2020).
38. F. Peng, M. I. Setyawati, J. K. Tee, X. Ding, J. Wang, M. E. Nga, H. K. Ho, D. T. Leong, Nanoparticles promote in vivo breast cancer cell intravasation and extravasation by inducing endothelial leakiness. *Nat. Nanotechnol.* **14**, 279–286 (2019).

39. W. Poon, B. R. Kingston, B. Ouyang, W. Ngo, W. C. W. Chan, A framework for designing delivery systems. *Nat. Nanothechnol.* **15**, 819–829 (2020).

40. Y. Li, W. Li, W. E. Bao, B. Liu, D. Li, Y. Jiang, W. Wei, F. Ren, Bioinspired peptosomes with programmed stimuli-responses for sequential drug release and high-performance anticancer therapy. *Nanoscale* **9**, 9317–9324 (2017).

41. Y. Chen, A. C. Munteanu, Y.-F. Huang, J. Phillips, Z. Zhu, M. Mavros, W. Tan, Mapping receptor density on live cells by using fluorescence correlation spectroscopy. *Chem. Eur. J.* **15**, 5327–5336 (2009).

42. Z. Shen, H. Ye, X. Yi, Y. Li, Membrane wrapping efficiency of elastic nanoparticles during endocytosis: Size and shape matter. *ACS Nano* **13**, 215–228 (2018).

43. L. Treuel, X. Jiang, G. U. Nienhaus, New views on cellular uptake and trafficking of manufactured nanoparticles. *J. R. Soc. Interface* **10**, 20120939 (2012).

44. K. Kettler, P. Krystek, C. Giannakou, A. J. Hendriks, W. H. de Jong, Exploring the effect of silver nanoparticle size and medium composition on uptake into pulmonary epithelial 16HBE14o-cells. *J. Nanopart. Res.* **18**, 182 (2016).

Citation: W. Bao, F. Tian, C. Lyu, B. Liu, B. Li, L. Zhang, X. Liu, F. Li, D. Li, X. Gao, S. Wang, W. Wei, X. Shi, Y. Li, Experimental and theoretical explorations of nanocarriers' multistep delivery performance for rational design and anticancer prediction. *Sci. Adv.* **7**, eaba2458 (2021).